A planar surface acoustic wave micropump for closed-loop microfluidics

R. Rimsa, A. J. Smith, C. Wälti, and C. D. Wood

Citation: Appl. Phys. Lett. **111**, 234102 (2017);
View online: https://doi.org/10.1063/1.5007701
View Table of Contents: http://aip.scitation.org/toc/apl/111/23
Published by the American Institute of Physics

A planar surface acoustic wave micropump for closed-loop microfluidics

R. Rimsa, A. J. Smith, C. Wälti, and C. D. Wood[a)]
School of Electronic and Electrical Engineering, University of Leeds, Woodhouse Lane, LS2 9JT Leeds, United Kingdom

(Received 2 October 2017; accepted 15 November 2017; published online 6 December 2017)

We have designed and characterized a simple Rayleigh-surface acoustic wave-based micropump, integrated directly with a fully enclosed 3D microfluidic system, which improves significantly the pumping efficiency within a coupled fluid whilst maintaining planar integration of the micropump and microfluidics. We achieve this by exploiting the Rayleigh-scattering angle of surface acoustic waves into pressure waves on contact with overlaid fluids, by designing a microfluidic channel aligned almost co-linearly with the launched pressure waves and by minimizing energy losses by reflections from, or absorption within, the channel walls. This allows the microfluidic system to remain fully enclosed—a pre-requisite for point-of-care applications—removing sources of possible contamination, whilst achieving pump efficiencies up to several orders of magnitude higher than previously reported, at low operating powers of 0.5 W. https://doi.org/10.1063/1.5007701

The ability to conduct experiments within miniaturized, self-contained platforms provides significant advantages such as reduced sample volumes, highly controlled reaction environments, and increased sensitivity, *inter alia*, offering potential benefits to applications in, for example, diagnostics,[1] sensing,[2,3] and synthesis.[4] Many such lab-on-chip (LOC) devices require controllable manipulation of fluids or suspensions around microfluidic channels. Historically, this has been achieved using external pumps, from which interconnects must be formed using often complex networks of fluidic and electrical assemblies.[5,6] The appeal of integrating pumping capabilities into the LOC platform using micropump technology is therefore driven primarily by the desire to increase portability [e.g., for point-of-care (PoC) diagnostics] by reducing the size, complexity, power requirements, and system costs.

Micropumps have been realized using several techniques, including electro-osmosis,[7] Quake valves,[8] and piezoelectric membranes,[9] although they generally still rely upon complex driving equipment that limits their portability.[5] One technology that seems to be particularly suited to LOC integration is based on Rayleigh surface acoustic waves (RSAWs). RSAWs are mechanical waves, a few nanometers in amplitude, generated at the surface of piezoelectric materials by the application of high-frequency electric signals to lithographically patterned, interdigitated transducers (IDTs), and can be driven using simple, portable circuits.[10,11] The RSAW is confined within a thin region (∼ one SAW wavelength) at the substrate surface and features an out-of-plane mechanical component which can couple strongly into longitudinal pressure waves within an overlaid fluid. These can be exploited to, for example, actuate micro-droplets,[12] align suspended particles,[13–15] achieve acoustophoretic particle separation,[16] and actively mix materials within microreactors in which mixing is otherwise diffusion limited.[17] Moreover, RSAWs can be used to pump liquids around both *open*[18,19] and *closed*[11,20,21] microfluidic systems, with the latter being a key tool for minimizing contamination in PoC devices.

Micropumps can be integrated with a broad range of microfluidic channel materials, including glass,[21] acrylic,[11] and polydimethylsiloxane (PDMS),[20] the latter often favored owing to its low cost (enabling single-use platforms where fouling and/or cross-contamination is a concern), its rapid prototyping capabilities, and its gas permeability (particularly advantageous for applications such as the "organ-on-chip").[22–24] However, commercial uptake of RSAW micropumps has been limited,[25] primarily owing to the low pressure gradients achievable within *closed* fluidic systems when using externally positioned electrodes (owing to acoustic losses at the channel interface)[21] or by electrode fouling and electrochemical reactions at the surface of electrodes when directly in contact with overlaid fluids. These issues can be mitigated by exciting RSAWs on a substrate separated from the microfluidic channel and subsequently coupling energy into the fluid through an intermediate coupling medium.[11] However, this can introduce further complications, including reduced operating times (owing to evaporation of the coupling medium) and, most importantly for PoC devices, provides a possible route for introducing contamination. In order to maintain a closed microfluidic system, planar integration of the RSAW with the channel is therefore preferable, and thus, a new solution is required.

On contact with a fluid, an RSAW is refracted into the liquid at the Rayleigh angle, in this case 22° from the surface normal[26] [Fig. 1(a)]. Hence, the majority of RSAW energy is coupled into near-vertical fluidic pressure waves. We present an RSAW micropump that exploits this phenomenon to maximize coupling efficiency into liquid pressure waves using a technique that, critically, avoids the need for either a separate substrate or a coupling medium. This arrangement generates extremely high pressure gradients and improvements in power efficiency, within *completely enclosed* microfluidic

a)Author to whom correspondence should be addressed: C.D.Wood@leeds.ac.uk.

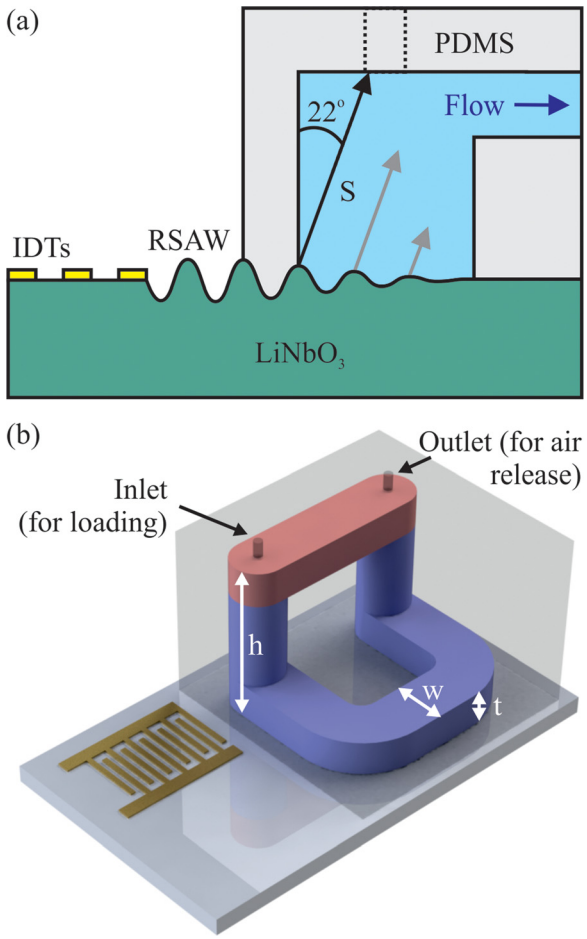

FIG. 1. Schematic illustration (not to scale) of (a) an RSAW scattering into a fluidic pressure wave at the Rayleigh angle of $\theta = 22°$, where S is the maximum propagation distance of the induced pressure wave within the fluidic channel, and (b) representative illustration of a fully assembled micropump device of width w, height h, depth t, and total length 15 mm. The red area, which forms the raised fluidic region, indicates the position at which an ABS tube was glued onto the underlying 3D-printed mould used to form the rest of the racetrack channel (blue).

channels, of up to several orders-of-magnitude beyond other reported RSAW-based micropumps, whilst operating at low ($\leq$0.5 W) applied powers. This was achieved by using three-dimensional microfluidic channels [Fig. 1(b)], by minimizing device losses, and by empirically selecting the most appropriate RSAW operating wavelength to optimize pump operation. We use this platform to perform a critical analysis of the state-of-the-art in RSAW micropump technology.

Devices were fabricated on X-propagating, 128° Y-cut "black" lithium niobate ($LiNbO_3$ Precision Micro-Optics Inc. MA, USA). All IDTs were patterned with a 1:1 mark-to-space ratio and comprised a 5 nm Ti adhesion layer coated with 50 nm of Au, formed using standard photolithography. Devices comprised either a single IDT (for fluid actuation) or a pair of opposing IDTS (for loss characterization). Molds for the lower-layer and vertical microfluidic channel sections [blue regions, Fig. 1(b)] were constructed from Spot-HT resin (Spot-A materials, Spain) using a stereolithographic 3D printer (Miicraft, Young Optics, Taiwan). A 0.5-mm-wide acrylonitrile butadiene styrene (ABS) plastic tube [red section, Fig. 1(b)] was cut to ~5 mm length, manually aligned to bridge the vertical pillars of the 3D printed mold and fixed into position using acetone. Microfluidic channels were cast from PDMS (1:10 base to cross-linker), which was degassed at a pressure of 5 mBar for 20 min. Prior to casting PDMS over the mold, the resin surface was passivated by depositing a fluorocarbon film in a reactive-ion etcher[27–29] (low pressure CHF_3 for 120 s at an RF power of 45 W). PDMS was next cast onto the passivated molds and baked at 70 °C for 1 h. The cured material was then peeled from the mold and sonicated for 20 min in acetone to dissolve the embedded ABS tube and thereby produce a fully 3D fluidic channel of dimensions $w = 500\,\mu$m, $t = 100\,\mu$m, and $h = 1.3$ mm [Fig. 1(b)]. The total channel length was fixed at $L = 15$ mm for all devices. The channel was cleaned with IPA prior to being oxygen-plasma-bonded onto the lithium niobate substrate, adjacent to the patterned IDTs and aligned to the acoustic aperture (defined by the IDT finger overlap). The complete device was glued onto a PCB using a thermally conductive adhesive, and electrical connections were made between the device and PCB using an Au ball bonder. To allow the channel to be loaded with the material, syringe needles (26 gauge, 0.46 mm outer diameter) were used to pierce temporary inlet and outlet holes. Once loaded, the needles were removed and the elastomeric properties of the PDMS caused the holes to close.

High-frequency signals, used to generate RSAWs, were produced using a signal generator (2022E, Marconi Instruments, UK) and amplifier (ZHL-1-2, Mini-circuits, USA). In order to assess flow rates (and therefore pressure gradients) within the channel, 2-μm-diameter fluorescent latex beads (Sigma-Aldrich, UK) were suspended in a solution comprised 0.1% v/v Triton in either pure DI water or a DI water/ethylene glycol mixture (3:1 molar ratio)—a viscous solution used to slow down particles for tracking, as required.[30] The particles were viewed using an upright fluorescence microscope (Olympus BX61, Olympus, UK), and their velocities were tracked using a 62.5 fps CCD camera (Rolera EM-C2, Q-imaging, Canada) combined with free imaging software.[31,32]

In order to choose an appropriate RSAW wavelength, λ_{SAW}, for micropump operation, two principle criteria must be considered. First, to maximize the pressure gradient induced within a coupled microfluidic system, the coupling efficiency from the RSAW mechanical energy into the fluidic pressure wave must be optimized. Second, possible RSAW losses must be minimized, including those arising from absorption at the PDMS-substrate interface, from the electrical impedance mismatch and from propagation losses into leaky bulk modes. The first criteria may be assessed analytically by calculating the SAW energy absorbed within a liquid, as defined by

$$\alpha = 1 - e^{-\beta(\omega)S}, \tag{1}$$

where S is the propagation distance of the induced pressure wave within the liquid [Fig. 1(a)] and $\beta(\omega)$ is the wavelength-dependent attenuation coefficient of an acoustic wave in a liquid.[11] For a channel depth h (equal to 1.3 mm in our vertical coupling section), S and $\beta(\omega)$ are given by, respectively

$$S = \frac{h}{\cos 22^0} \tag{2}$$

and

$$\beta(\omega) = \frac{b\omega^2}{2\rho c^3}, \tag{3}$$

where ρ is the liquid density, ω is the SAW angular frequency, c is the liquid sound velocity, and b is given by

$$b = \left(\frac{4}{3}\mu + \mu_0\right), \tag{4}$$

where μ and μ_0 are the liquid shear and bulk viscosity, respectively. As an example, the coupling efficiency as a function of λ_{SAW} is calculated for a water-filled channel [Fig. 2(a)], for which $\mu = 0.888$ mPa s, $\mu_0 = 2.469$ mPa s,[33] $\rho = 1000\,\mathrm{kg/m^3}$, and $c = 1480\,\mathrm{m/s}$. Across the wavelength range 20–125 μm, the coupling efficiency is observed to decrease by over an order of magnitude. Furthermore, $\lambda_{SAW} = 125\,\mu$m corresponds to an RSAW wavelength approximately one quarter of the substrate thickness, after which point leaky bulk modes are likely to propagate, and therefore, transducers with longer wavelengths were not investigated. Although shorter wavelengths appear to offer increasingly better coupling into the fluid, a short wavelength limit of 20 μm (equivalent to the 5 μm electrode finger and gap width) was imposed to maintain ease of fabrication. Within this range, ten devices were designed with wavelengths of 20, 25, 30, 40, 50, 60, 70, 80, 100, and 125 μm (corresponding to fundamental operating frequencies of 195.4, 156.3, 130.3, 97.7, 78.2, 65.1, 55.8, 48.9, 39.1, and 31.3 MHz, respectively, assuming a SAW velocity of 3980 m/s).

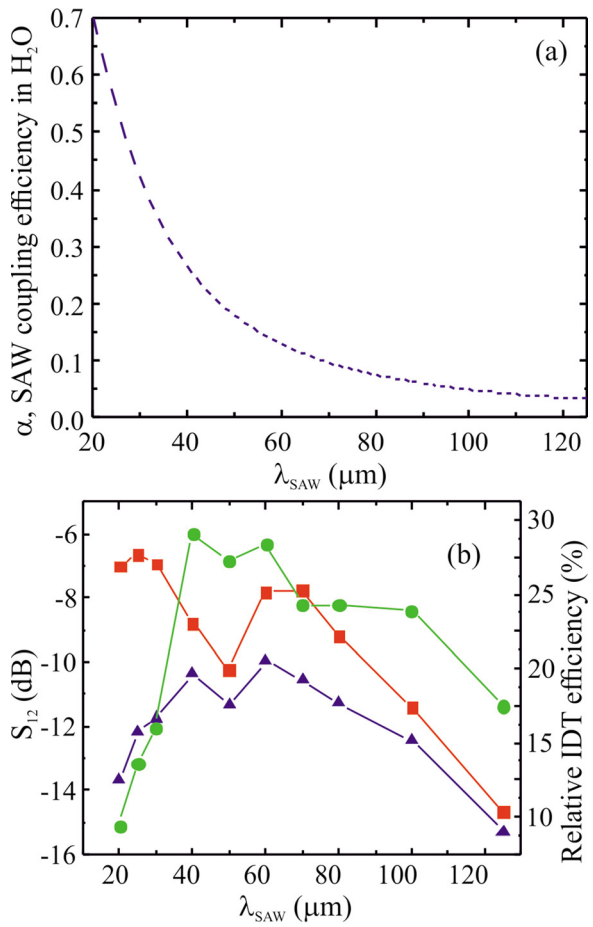

FIG. 2. (a) RSAW coupling efficiency in liquid as a function of wavelength, and (b) device insertion loss, measured using 2-port devices, for both unloaded devices (red squares) and devices loaded with a PDMS wall between opposing transducers (blue triangles), both plotted against the left-hand y-axis. The relative transducer efficiency corresponds to the ratio of loaded-to-unloaded insertion loss (green circles, right hand y-axis). Lines are drawn as a guide to the eye.

To maximize coupling between the driving electronics and the RSAW (i.e., to reduce insertion loss), each IDT impedance, R_{in}, was designed to be 50 Ω using[34]

$$R_{in} = \frac{1}{H_a}\left(\frac{1}{2f_0 C_s N_p}\right)\frac{4k^2 N_p}{4k^2 N_p + \pi^2}, \tag{5}$$

where H_a is the acoustic aperture width, R_0 is the fundamental operating frequency, N_p is the number of finger pairs per IDT, C_s is the material static capacitance, and k is the piezoelectric coupling coefficient. To facilitate ease of alignment between the 500-μm-wide microfluidic channels and the IDTs, an alignment tolerance of ±150 μm was chosen, resulting in a minimum $H_a = 800\,\mu$m for all devices. Therefore, according to Eq. (5), to maintain $R_{in} = 50\,\Omega$ for each λ_{SAW}, the number of finger pairs within each IDT must be varied as shown in Table I, which also contains the corresponding device operating frequencies and acoustic aperture sizes. All impedances were within an acceptable range of 45–55 Ω. Device operating frequencies were observed ubiquitously to lie below their corresponding design frequencies, a result of mass-loading by the gold electrodes.

Owing to the elastomeric properties of PDMS, SAWs propagating beneath a PDMS layer experience significant attenuation. In order to implement a closed-loop channel using PDMS, this attenuation was therefore minimized by reducing the channel wall thickness immediately adjacent to the acoustic aperture, from 1 mm (for the rest of the channel) to 156 ± 9 μm (the resolution limit of our 3D printer). Furthermore, the wavelength-dependent attenuation was quantified by measuring transmission (S_{12}) parameters using separate, two-port RSAW devices fabricated at each value of λ_{SAW}, both with [Fig. 2(b), red squares] and without [Fig. 2(b), blue triangles] a 156-μm-thick PDMS barrier positioned between opposing IDTs. This allowed the PDMS-induced attenuation, $\zeta_{PDMS} = S_{12,unloaded} - S_{12,PDMS}$ (in dB) to be measured empirically. However, since the insertion loss varies significantly between devices, a more useful parameter to characterize is the relative electrode efficiency, η_{rt} [green circles, Fig. 2(b)] calculated using

TABLE I. Measured operating frequency, acoustic aperture widths, and finger pair count chosen to ensure a 50 Ω impedance for the selected SAW micropump design wavelengths.

λ_{SAW}, μm	f_0 (MHz)	H_a (μm)	N_p
20	193.6	748	20
25	155.2	935	25
30	129.6	815	25
40	96.0	814	30
50	77.6	785	35
60	65.0	745	40
70	55.7	869	40
80	48.8	803	45
100	38.9	1000	45
125	31.8	1030	50

$$\eta_{rt} = 100 \times 10^{\frac{0.5S_{12}+\zeta_{PDMS}}{10}}. \quad (6)$$

The electrode efficiency is observed to peak in the range of $\lambda_{SAW} = 40$–$60\,\mu$m. Longer wavelength devices suffer from decreased electrode efficiency and increased mass loading,[35,36] whereas the steep roll-off at shorter wavelengths arises from increased absorption within the PDMS channel wall [analogous to increased coupling into the overlaid material, similar to that observed in Fig. 2(a) for water]. Devices operating at wavelengths shorter than $30\,\mu$m were therefore not considered further.

The performance of each RSAW pump was characterized by inferring the induced liquid flow rate from the velocities of a suspension of fluorescent latex particles. These were measured using Trackmate, which produced particle trajectories from recordings of the induced flow. Flow profiles were then generated [supplementary material, Figs. S1(a)–S1(h)] by averaging the measured particle velocities ($n = 1000$) within artificially defined channel regions lying parallel to the flow direction (supplementary material, Fig. S2), confirming pressure-driven flow for all devices.[20] Although the volume flow rate is often quoted directly to demonstrate pumping performance, this is only useful when comparing equivalent channel geometries and liquid viscosities; a more generalized parameter is the pressure gradient, calculated using[37]

$$G = \frac{u(y,z)\mu w}{4\sum_{n=1}^{\infty}\frac{(-1)^{n+1}}{\kappa_n^3}\left(1-\frac{\cosh(\kappa_n z)}{\cosh(0.5\kappa_n t)}\right)\cos(\kappa_n y)}, \quad (7)$$

where $\kappa = (2n-1)\pi/w$, $\mu = 3.69$ mPa s or $\mu = 1.0$ mPa s is the shear viscosity of the glycerol-water mixture (for $\lambda_{SAW} \leq 70\,\mu$m) or water (for $\lambda_{SAW} > 70\,\mu$m), respectively, w and t are the channel width and depth, and $u(y,z)$ is the maximum measured particle velocity, dependent on z (the vertical position within the channel with respect to the substrate plane) and y (the lateral position across the channel width). An empirically measured maximum for $u(y,z)$ was found to occur at $y = 0$, $z = 35\,\mu$m, approximately at the vertical centre of the channel within the focal depth of the microscope objective. This focal plane was therefore maintained for all experiments. The values of $u(y,z)$ were calculated by performing a least squares fit ($\chi^2 > 0.999$) of Eq. (7) to the measured flow velocity profiles for each device and applied power (supplementary material, Fig. S1). The pressure gradient, which is a measure of pumping performance, was then calculated for each device and plotted as a function of applied power in Fig. 3. The maximum applied power was limited to 0.5 W for the 40, 50, and $60\,\mu$m wavelength devices to avoid bubble formation within the liquid, caused by cavitation at very high pressure gradients.[37] The inset of Fig. 3 shows the dependence of the pressure gradient on SAW wavelength at a fixed applied power of 0.5 W, showing a pronounced maximum at $40\,\mu$m. The optimal performance of this device is attributed to a combination of maximal power transmission beneath the PDMS channel wall at $\lambda_{SAW} = 40\,\mu$m [see Fig. 2(b)] whilst maintaining a relatively high SAW–liquid coupling efficiency [Fig. 2(a)].

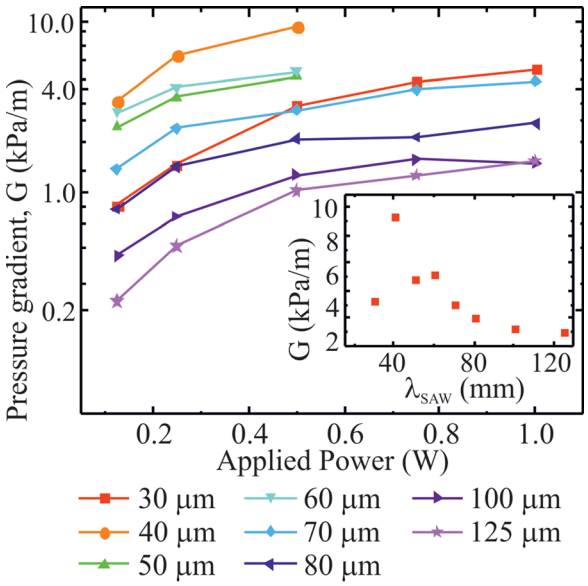

FIG. 3. Pressure gradient versus applied power for SAW devices operating at different wavelengths. Inset: Generated pressure gradient as a function of SAW wavelength at a fixed applied power of 0.5 W.

The delivered power is given by $P_{del} = pQ$, where Q is the volume flow rate given by[37]

$$Q = \frac{8Gt}{\mu w}\sum_{n=1}^{\infty}\frac{1}{\kappa_n^4}\left(1-\frac{2}{\kappa_n t}\tanh\left(\frac{\kappa_n t}{2}\right)\right), \quad (8)$$

in which the channel depth $t = 100\,\mu$m and p is the pressure difference between the channel inlet and outlet. Assuming a linear pressure gradient along the channel length, p can be estimated using $p = GL$. To compare with existing RSAW-based micropumps, the power efficiency can be calculated using $\eta = \frac{P_{del}}{P_{app}}$, where P_{app} is the applied power. Figure 4 shows the power efficiency of a water-filled fluidic channel as a function of applied power for devices operating between 40 and $60\,\mu$m, in comparison to the best RSAW micropumps reported to date.[11,20,21] Over the applied power range used here, we achieved significantly higher power efficiencies within our closed-loop devices than that has been previously reported under equivalent operating conditions. For example, at an applied power of 0.5 W, for $\lambda_{SAW} = 40\,\mu$m, we achieve a power efficiency of 1.22×10^{-7}, almost an order of magnitude greater than the best published performance of $< 2.6 \times 10^{-8}$ achieved at the same input power and more than double the highest reported efficiency, which required a driving power of 2.6 W. The ratio is even higher at lower applied powers, an important characteristic for portable applications.

In conclusion, we have developed a SAW-based micropump that allows the use of a closed microfluidic system that can exploit the benefits of using PDMS, whilst overcoming pumping limitations encountered previously in RSAW-driven, closed-loop microfluidic channels. We achieved this by exploiting the Rayleigh-scattering of SAWs into fluids to maximize energy coupling into fluidic pressure waves and by maximizing the electrical power delivered to our devices by impedance matching, combined with determining a workable compromise between minimizing elastic-losses at the

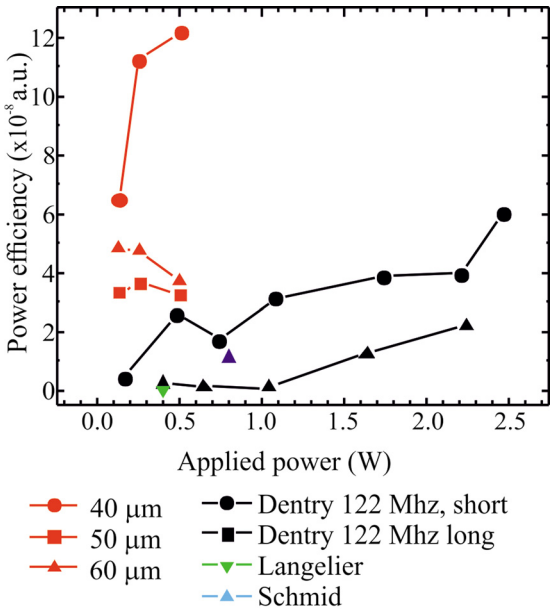

FIG. 4. Power efficiency versus applied power in a water-filled channel, for devices operating at wavelengths of 40, 50, and 60 μm, in comparison to literature values for power efficiency from the studies by Dentry *et al.*,[11] Schmid *et al.*,[20] and Langeleir *et al.*[21]

PDMS channel interface whilst maximizing SAW-fluid coupling efficiency. This resulted in at least an order-of-magnitude increase in pumping power efficiency compared to that which has been previously reported using such technology. Whilst further improvements could be made by, for example, improving the relative transducer efficiency and using less absorbing materials, this work demonstrates a significant step towards the implementation of RSAW micropumps in PoC devices.

See supplementary material for the velocity of 2 μm latex spheres measured as a function of position across the microfluidic channel for applied powers in the range of 0.125–1.00 W, repeated for RSAW devices operating at wavelengths between 30 and 125 μm (Fig. S1). Each point represents an average velocity (n = 1000) with error bars representing standard deviations. Figure S2 provides an example of how the microfluidic channel is sectioned into discrete regions, within which average particle velocities are tracked in order to produce flow profiles across the microfluidic channel.

This work was funded by the EPSRC Centre for Doctoral Training in Molecular-Scale Engineering (EP/J001244/1) and Wellcome Trust (201058/Z/16/Z). Data used in producing this work can be accessed via the University of Leeds Data Repository.[38]

[1]E. K. Sackmann, A. L. Fulton, and D. J. Beebe, Nature **507**, 181 (2014).
[2]K. Ohno, K. Tachikawa, and A. Manz, Electrophoresis **29**, 4443 (2008).
[3]J. Wu and M. Gu, J. Biomed. Opt. **16**, 80901 (2011).
[4]K. S. Elvira, X. C. I. Solvas, R. C. R. Wootton, and A. J. deMello, Nat. Chem. **5**, 905 (2013).
[5]A. K. Au, H. Lai, B. R. Utela, and A. Folch, Micromachines **2**, 179 (2011).
[6]L. Y. Yeo and J. R. Friend, Annu. Rev. Fluid Mech. **46**, 379 (2014).
[7]S. Zeng, C. H. Chen, J. C. Mikkelsen, and J. G. Santiago, Sens. Actuators, B **79**, 107 (2001).
[8]M. A. Unger, H. P. Chou, T. Thorsen, A. Scherer, and S. R. Quake, Science **288**, 113 (2000).
[9]M. C. Tracey, I. D. Johnston, J. B. Davis, and C. K. L. Tan, J. Micromech. Microeng. **16**, 1444 (2006).
[10]L. Y. Yeo and J. R. Friend, Biomicrofluidics **3**, 12002 (2009).
[11]M. B. Dentry, J. R. Friend, and L. Y. Yeo, Lab Chip **14**, 750 (2014).
[12]A. Wixforth, Superlattices Microstruct. **33**, 389 (2003).
[13]C. D. Wood, S. D. Evans, J. E. Cunningham, R. O'Rorke, C. Wälti, and A. G. Davies, Appl. Phys. Lett. **92**, 44104 (2008).
[14]C. D. Wood, J. E. Cunningham, R. O'Rorke, C. Wälti, E. H. Linfield, A. G. Davies, and S. D. Evans, Appl. Phys. Lett. **94**, 54101 (2009).
[15]X. Ding, S.-C. S. Lin, B. Kiraly, H. Yue, S. Li, I.-K. Chiang, J. Shi, S. J. Benkovic, and T. J. Huang, Proc. Natl. Acad. Sci. U.S.A. **109**, 11105 (2012).
[16]D. J. Collins, A. Neild, and Y. Ai, Lab Chip **16**, 471 (2016).
[17]R. J. Shilton, L. Y. Yeo, and J. R. Friend, Sens. Actuators, B **160**, 1565 (2011).
[18]S. Girardo, M. Cecchini, F. Beltram, R. Cingolani, and D. Pisignano, Lab Chip **8**, 1557 (2008).
[19]M. Tan, L. Yeo, and J. Friend, EPL (Europhys. Lett.) **87**, 47003 (2009).
[20]L. Schmid, A. Wixforth, D. A. Weitz, and T. Franke, Microfluid. Nanofluid. **12**, 229 (2012).
[21]S. M. Langelier, L. Y. Yeo, and J. Friend, Lab Chip **12**, 2970 (2012).
[22]S. Halldorsson, E. Lucumi, R. Gómez-Sjöberg, and R. M. T. Fleming, Biosens. Bioelectron. **63**, 218 (2015).
[23]A. Jain, A. Graveline, A. Waterhouse, A. Vernet, R. Flaumenhaft, and D. E. Ingber, Nat. Commun. **7**, 10176 (2016).
[24]N. S. Bhise, V. Manoharan, S. Massa, A. Tamayol, M. Ghaderi, M. Miscuglio, Q. Lang, Y. Shrike Zhang, S. R. Shin, G. Calzone, N. Annabi, T. D. Shupe, C. E. Bishop, A. Atala, M. R. Dokmeci, and A. Khademhosseini, Biofabrication **8**, 14101 (2016).
[25]A. Winkler, R. Brunig, C. Faust, R. Weser, and H. Schmidt, Sens. Actuators, A **247**, 259 (2016).
[26]M. B. Dentry, L. Y. Yeo, and J. R. Friend, Phys. Rev. E **89**, 13203 (2014).
[27]H. N. Chan, Y. Chen, Y. Shu, Y. Chen, Q. Tian, and H. Wu, Microfluid. Nanofluid. **19**(1), 9 (2015).
[28]V. Saggiomo and A. H. Velders, Adv. Sci. **2**, 1500125 (2015).
[29]G. Comina, A. Suska, and D. Filippini, Lab Chip **14**, 424 (2014).
[30]T. Sun and A. S. Teja, J. Chem. Eng. Data **48**, 198 (2003).
[31]J.-Y. Tinevez, N. Perry, J. Schindelin, G. M. Hoopes, G. D. Reynolds, E. Laplantine, S. Y. Bednarek, S. L. Shorte, and K. W. Eliceiri, Methods **115**, 80 (2017).
[32]J. Schindelin, I. Arganda-Carreras, E. Frise, V. Kaynig, M. Longair, T. Pietzsch, S. Preibisch, C. Rueden, S. Saalfeld, B. Schmid, J.-Y. Tinevez, D. J. White, V. Hartenstein, K. Eliceiri, P. Tomancak, and A. Cardona, Nat. Methods **9**, 676 (2012).
[33]M. J. Holmes, N. G. Parker, and M. J. W. Povey, J. Phys. Conf. Ser. **269**, 012011 (2010).
[34]W. Wilson and G. Atkinson, NASA Technical Reports No. 1, 2007.
[35]G. A. Coquin and H. F. Tiersten, J. Acoust. Soc. Am. **41**, 921 (1967).
[36]K. Dransfeld and E. Salzmann, in *Physical Acoustics Principles and Methods* edited by W. P. Mason and R. N. Thurston (Academic Press, New York, NY, 1970), Vol. 7, pp. 219–270.
[37]P. Tabeling, *Introduction to Microfluidics* (Oxford University Press, Oxford, 2005).
[38]R. Rimsa, A. J. Smith, C. Wälti, and C. D. Wood, "A planar surface acoustic wave micropump for closed loop microfluidics," Dataset. https://doi.org/10.5518/232 (2017).